

An estimation of the *Gaia* EDR3 parallax bias from stellar clusters and Magellanic Clouds data

J. Maíz Apellániz¹

Centro de Astrobiología, CSIC-INTA. Campus ESAC. C. bajo del castillo s/n. E-28 692 Villanueva de la Cañada, Madrid, Spain
e-mail: jmaiz@cab.inta-csic.es

Received 4 October 2021 / Accepted 4 November 2021

ABSTRACT

Context. The early-third *Gaia* data release (EDR3) parallaxes constitute the most detailed and accurate dataset that currently can be used to determine stellar distances in the solar neighborhood. Nevertheless, there is still room for improvement in their calibration and systematic effects can be further reduced in some circumstances.

Aims. The aim of this paper is to determine an improved *Gaia* EDR3 parallax bias as a function of magnitude, color, and ecliptic latitude using a single method applied to stars in open clusters, globular clusters, the Large Magellanic Cloud (LMC), and the Small Magellanic Cloud (SMC).

Methods. I study the behavior of the residuals or differences between the individual (stellar) parallaxes and the group parallaxes, which are assumed to be constant for the corresponding cluster or galaxy. This was done by first applying the Lindegren et al. (2021) zero point and then calculating a new zero point from the residuals of the first analysis.

Results. The Lindegren zero point shows very small residuals as a function of magnitude between individual and group parallaxes for $G > 13$ but significant ones for brighter stars, especially blue ones. The new zero point reduces those residuals, especially in the $9.2 < G < 13$ range. The k factor that is used to convert from catalog parallax uncertainties to external uncertainties is small (1.1-1.7) for $9.2 < G < 11$ and $G > 13$, intermediate (1.7-2.0) for $11 < G < 13$, and large (> 2.0) for $G < 9.2$. Therefore, significant corrections are needed to calculate distance uncertainties from *Gaia* EDR3 parallaxes for some stars. There is still room for improvement if future analyses add information from additional stellar clusters, especially for red stars with $G < 11$ and blue stars with $G < 9.2$. I also calculated k for stars with RUWE values between 1.4 and 8.0 and for stars with six-parameter solutions, allowing for a correct estimation of their uncertainties.

Key words. astrometry – globular clusters: general – open clusters and associations: general – methods: data analysis – parallaxes – stars: distances

1. Introduction

This is the second paper of a series on the validity of the parallaxes of the early third *Gaia* data release (EDR3; Brown et al. 2021), which was presented on 3 December 2020 and included parallaxes for $\sim 1.5 \times 10^9$ sources. Lindegren et al. (2021a), from now on L21a, presents the astrometric solution for *Gaia* EDR3 and Lindegren et al. (2021b), from now on L21b, derived the parallax bias (or zero point, Z_{EDR3}) in the data as a function of magnitude (G), the primary very broadband optical photometry provided by *Gaia*, color (v_{eff} , the effective wavenumber, which for most well-behaved sources is a function of the $G_{\text{BP}}-G_{\text{RP}}$ color provided by *Gaia*; see Fig. 2 in L21a), and ecliptic latitude (β). In the first paper of this series (Maíz Apellániz et al. 2021b, from now on Paper I) I used a variety of astrophysical sources to validate the results of L21a and L21b. In particular, I used *Gaia* EDR3 parallaxes for stars in globular clusters to test the Z_{EDR3} of L21b and determined that it works well for faint stars but that it can be improved for bright ones.

The method used in Paper I to validate Z_{EDR3} is based on the determination of distances to stellar groups from parallaxes established in Campillay et al. (2019) and Maíz Apellániz (2019) and developed in Maíz Apellániz et al. (2020), from now on Villafranca I. That paper is the first one of a series on the Villafranca catalog of OB groups, Those OB groups, together with those in

the second paper of the series (Villafranca II, described below), constitute an important part of the sample that is used in this paper. The analysis of Z_{EDR3} in Paper I uses the residual or difference between the individual parallaxes for each star and the parallax for the stellar group (in that paper, one of six globular clusters), ϖ_g , to determine if the individual parallaxes require a correction (given by Z_{EDR3}) or, if the correction has already been calculated, whether it has the expected properties or not. More specifically, I define the corrected individual parallaxes as:

$$\varpi_c = \varpi - Z_{\text{EDR3}} \quad (1)$$

and the residual or difference with the group parallax as:

$$\Delta\varpi = \varpi_c - \varpi_g. \quad (2)$$

The distribution of $\Delta\varpi$ normalized by its total or external uncertainty σ_{ext} should have a mean of zero and a standard deviation of one. The external uncertainty was calculated as follows:

$$\sigma_{\text{ext}} = \sqrt{k^2 \sigma_{\text{int}}^2 + \sigma_s^2}, \quad (3)$$

where σ_{int} is the internal (catalog) random uncertainty, σ_s is the systematic uncertainty, and k is a multiplicative constant

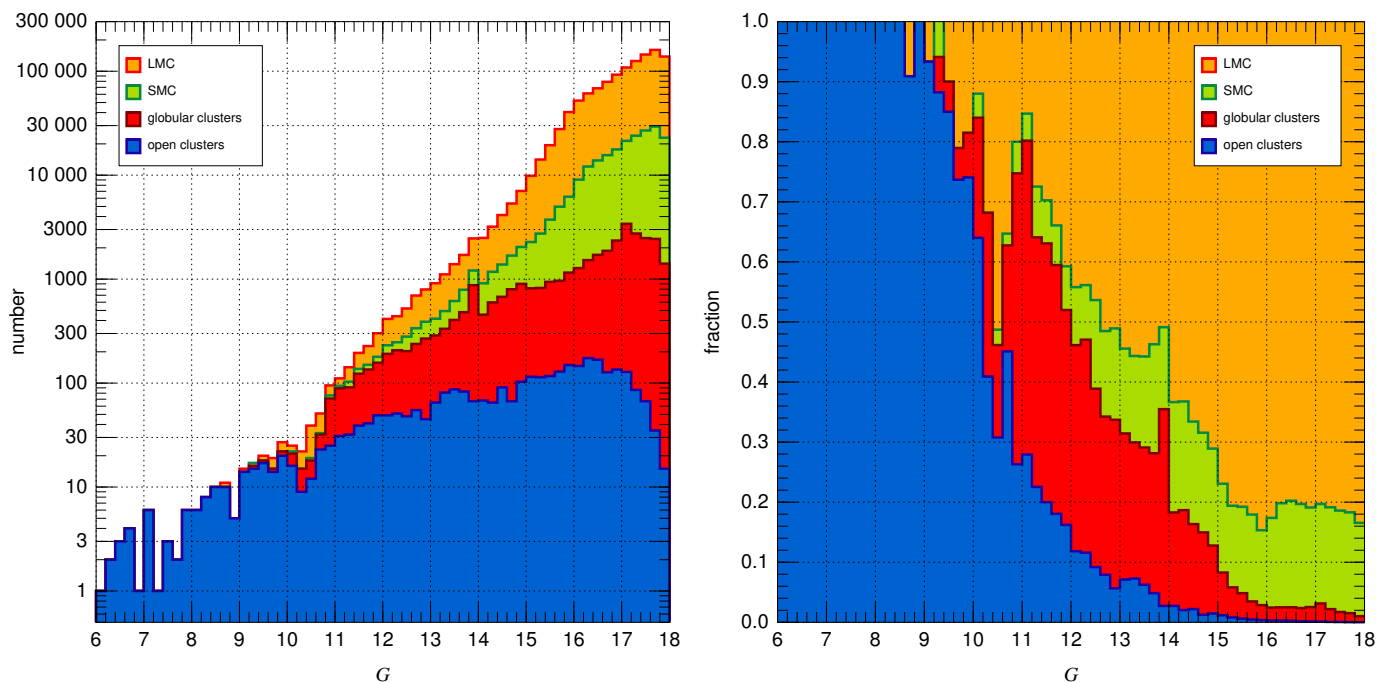


Fig. 1. (left) G magnitude histogram for the samples in this paper using 0.2 mag bins and with a logarithmic vertical scale. I note that the distribution of each sample is plotted above that of the following one, so the top line should be interpreted as the histogram for the total sample. (right) Fraction that each sample contributes per 0.2 mag bin.

that needs to be determined and that may depend on magnitude or other quantities. The value obtained for σ_s in Paper I was $10.3 \mu\text{as}$ and that is the value that is used here. For further details on the definitions, see Paper I.

In this paper I present new estimations of the *Gaia* EDR3 parallax bias and of k based on the analysis of the parallaxes of stars that belong to open clusters (from Villafranca I and II), globular clusters (from Paper I), and from the LMC and the SMC (from Luri et al. 2021). The new Z_{EDR3} relies on the absolute QSO zero point of L21b but is otherwise independent of their calculation. The new estimations are applicable only to stars with five-parameter astrometric solutions in the case of Z_{EDR3} but for k I extend the analysis to six-parameter astrometric solutions. In the next section I describe the data and methods and in the following one I present and analyze the results. I conclude with a summary and possible ways to expand this work.

2. Data and methods

2.1. How the sample was selected

As mentioned above, the sample in this paper is a combination of stars with good-quality *Gaia* EDR3 data from four types of objects: the LMC, the SMC, globular clusters, and open clusters. I first describe the selection process for the Magellanic Clouds and then I do it for the stellar clusters.

For the LMC and the SMC I start with the sample obtained by Luri et al. (2021), who used an iterative procedure to eliminate nonmembers. I then restrict the sample to those objects [a] within 10° of the respective galaxy centers, [b] with $\text{RUWE} < 1.4$ (Renormalized Unit Weight Error, see L21a), [c] with five-parameter *Gaia* EDR3 solutions (see L21a), and [d] with $\sigma_{\text{ext}} < 100 \mu\text{as}$ using the k and σ_s values from paper I. This leaves us with a total of 989 909 LMC stars and 196 413 SMC stars with good-quality *Gaia* EDR3 parallaxes. As there are few stars fainter than $G = 18$ mag among those and because of the

way the rest of the sample is selected, I add the additional condition [e] with $G < 18$ mag, leaving us with 950 696 LMC stars and 192 266 SMC stars.

For the globular clusters I use the sample from Paper I that consists of stars from six such systems (ω Cen, 47 Tuc, NGC 6752, M5, NGC 6397, and M13). The selection of the stars was performed applying the same [b] to [e] conditions as in the previous paragraph, with the total number of stars for the six globular clusters being 30 577, ranging from the 1154 in M5 to the 14 606 in 47 Tuc (I note that Table 5 in Paper I includes stars with six-parameter solutions, which are excluded here). The sample in each cluster is selected by position and proper motion and applying a 4σ cut in normalized parallax (see Paper I for details). The selection technique can be described as a simplified version as the one used by Luri et al. (2021), as globular clusters are more simple systems than the MCs and are also located at closer distances, which makes it easier to eliminate contaminants.

The sample for the open clusters¹ consists of stars from 26 such systems, named as Villafranca O-001 to Villafranca O-026. The first sixteen of those were originally defined in Villafranca I and the next ten were added in Villafranca II (Maíz Apellániz et al. 2021a). In that second paper the main criterion for adding OB groups to the list was precisely their usefulness for the analysis here, namely, the addition of a large number of stars per cluster with a high degree of certainty in membership. The sixteen Villafranca I OB groups were originally analyzed with *Gaia* DR2 astrometry but they were re-analyzed with *Gaia* EDR3 astrometry (together with the ten new groups) in Villafranca II. For the North America nebula I use Villafranca O-

¹ I use the term “open cluster” to refer to the OB groups defined in Villafranca I and II even though some of them are not strictly bound systems. However, for the purposes of this paper that is irrelevant, as their spread in distances introduces a dispersion in their parallaxes that is small in comparison with the effects I am trying to measure.

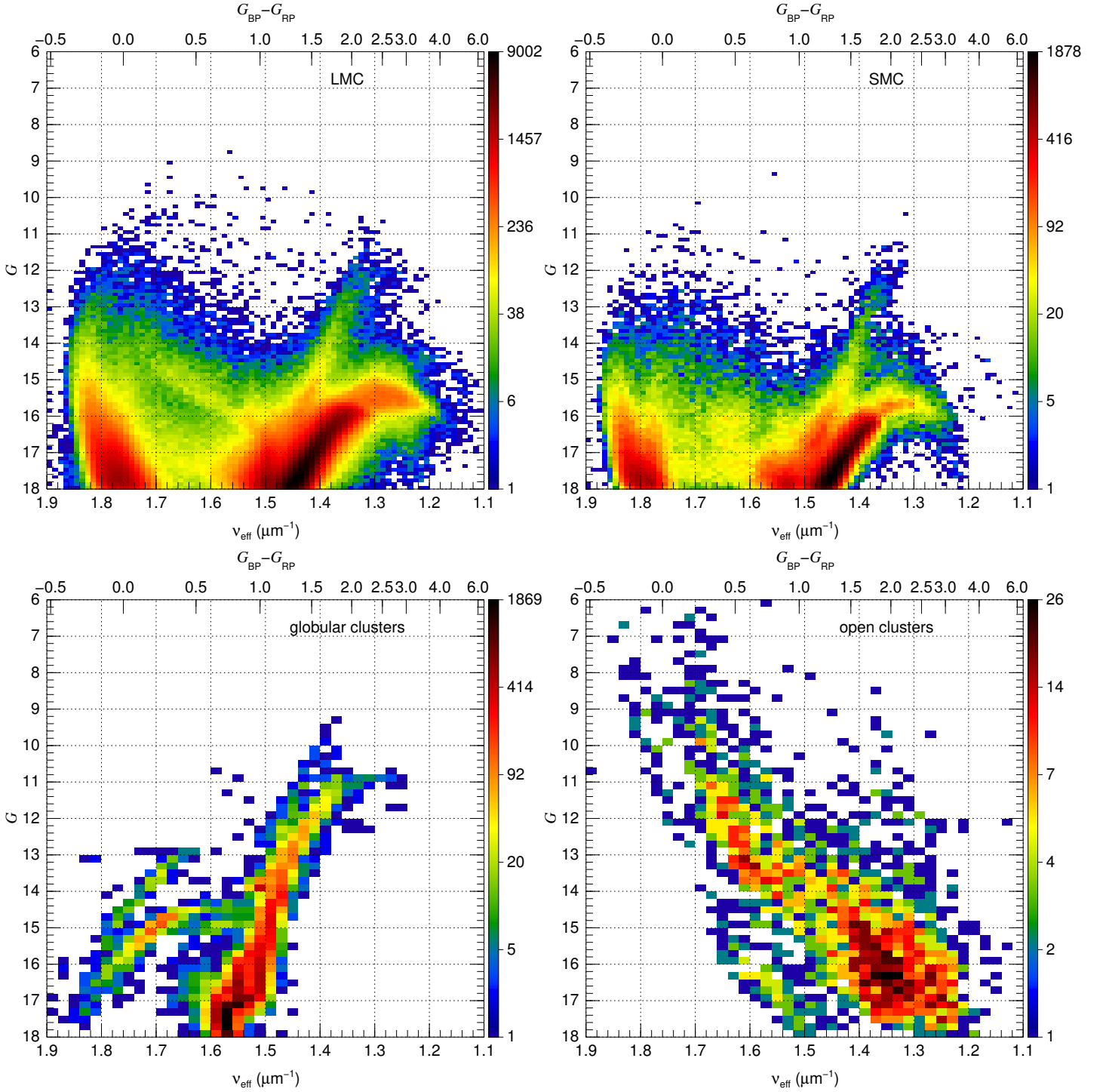


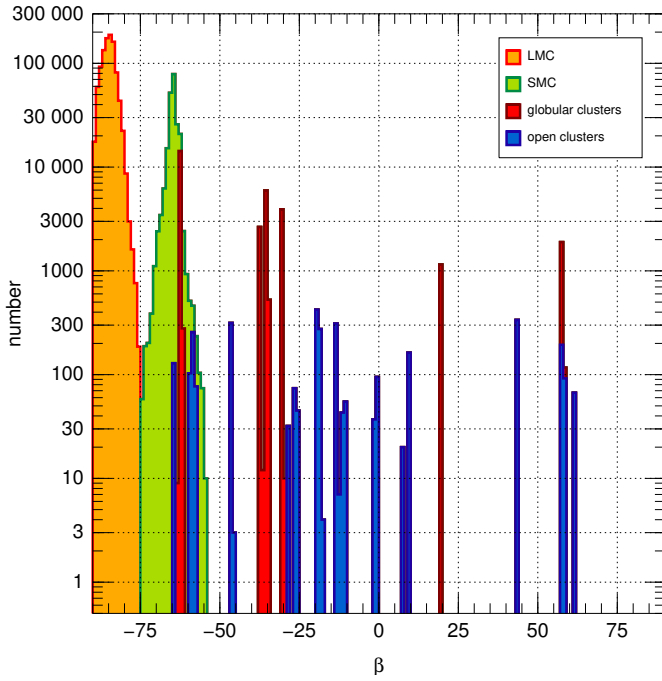
Fig. 2. CMDs for the LMC (upper left), SMC (upper right), globular cluster (lower left), and open cluster (lower right) samples. The intensity scale is logarithmic and the cell sizes are $0.01 \mu\text{m}^{-1} \times 0.1 \text{ mag}$ (upper panels) and $0.02 \mu\text{m}^{-1} \times 0.2 \text{ mag}$ (lower panels). The color bars at the right of each plot give the number of stars per cell, I note that they are very different from panel to panel. The upper x axes use Eqn. 4 of L21a to transform from v_{eff} to $G_{\text{BP}} - G_{\text{RP}}$.

014 NW as the cluster. The selection process of the sample in each open cluster is the same as that in Villafranca I and II and is similar to that of the globular clusters with two general differences: an additional cut using a displaced isochrone in the CMD is applied and the cut in normalized parallax is applied at 3σ instead of at 4σ . The reason behind the first difference is that OB groups are usually located close to the Galactic plane, where the field population is a stronger contaminant than for globular clus-

ters. The second difference arises from the lower number of stars selected per cluster, which ranges from 11 (Villafranca O-013) to 482 (Villafranca O-022), for a total of 3155 stars in open clusters (I note that the numbers in Villafranca I are from *Gaia* DR2, not *Gaia* EDR3, and that the statistics in both Villafranca papers also include stars with six-parameter solutions). Additionally, eleven stars that satisfied all requirements except that of the normalized parallax were added by hand because they are bright stars

Table 1. Stars in open clusters manually added to the sample.

<i>Gaia</i> EDR3 ID	Clus. ID	Star name	<i>G</i> (mag)	ν_{eff} (μm^{-1})
5 350 363 807 177 527 680	O-002	ALS 15 863	11.133	1.608
3 326 715 714 242 517 248	O-016	HD 47 755	8.443	1.797
4 146 612 425 449 995 648	O-019	ALS 15 369	11.217	1.486
3 131 327 653 265 431 552	O-020	HD 46 056 B	10.895	1.661
5 966 509 267 005 564 288	O-022	HDE 326 331 A	7.488	1.690
5 966 509 438 804 267 264	O-022	HD 152 314 Aa,Ab	7.802	1.680
5 966 508 957 767 911 040	O-022	HDE 326 330	9.546	1.685
3 017 364 063 330 465 152	O-023	θ^1 Ori D	6.583	1.715
3 017 360 348 171 372 672	O-023	HD 36 982	8.342	1.696
3 017 265 961 968 363 904	O-023	HD 36 939	8.968	1.758
5 350 310 927 535 609 728	O-025	CPD -59 2635	9.118	1.641

**Fig. 3.** β (ecliptic latitude) histogram for the samples in this paper using 1° bins and with a logarithmic vertical scale. I note that the distribution of each sample is plotted above that of the following one, so the top line should be interpreted as the histogram for the total sample.

that were excluded by a small margin and additional information suggests they are indeed cluster members. As we see below, their original exclusion was caused by the underestimation of k for bright stars in Paper I. The eleven stars are listed in Table 1.

2.2. Why the sample was selected

The first goal in this paper is to derive a new parallax zero point for the five-parameter solutions in *Gaia* EDR3 following the same parameter dependencies of L21b, that is:

$$Z_{\text{EDR3}}(G, \nu_{\text{eff}}, \beta) = \sum_{j=0}^4 \sum_{k=0}^2 q_{jk}(G) c_j(\nu_{\text{eff}}) b_k(\beta), \quad (4)$$

with the different terms explained in Appendix A of L21b and section 2 of Paper I. In summary, there are eight possible terms for a given magnitude G : q_{00} , q_{01} , q_{02} are the three color-

independent β terms; q_{10} , q_{20} , q_{30} , and q_{40} are the three β -independent color terms (with the first one applying to the intermediate color range where most stars are located, the next two to red stars, and the last one to blue stars); and q_{11} is the only term that depends on both color and β . Ideally, one should cover the $G + \nu_{\text{eff}} + \beta$ ranges of interest as thoroughly and uniformly as possible. In practice this is not possible for a number of reasons:

- In general, faint stars are more common than bright ones.
- Single-age populations follow quasi-one-dimensional distributions (isochrones) in a CMD.
- Stars are not uniformly distributed over the whole sky.
- The presence of contaminants should be minimized.

The approach in this paper is to use the four different samples described above to try to cover the three-dimensional space of interest as best as possible. To describe how that is done, I divide G in three ranges: faint ($13 < G < 18$), intermediate ($9.2 < G < 13$), and bright ($6 < G < 9.2$) and use Figs. 1, 2, and 3 to analyze how our sample is distributed.

The faint range is the better covered, as the LMC and SMC include objects of most magnitudes and colors and the small gaps left are well complemented with the other two samples. The issue with the LMC and SMC is that they are both located near the south ecliptic pole, so clusters are needed to extend the solution to other latitudes (Fig. 3).

In the intermediate range the coverage is not as good and here is where the presence of different types of samples becomes even more useful. For the fainter end of the range the MCs are still the dominant contribution but only for blue and red colors, not intermediate ones. As we move to brighter magnitudes in this range, globular clusters become the most common population but only for red stars. Finally, for objects brighter than $G = 10$ mag open clusters dominate but most of them are blue.

The worst coverage of all is for bright stars. The sample is very small and it is composed almost exclusively of blue stars in open clusters.

In summary, I expect Z_{EDR3} to be better characterized for faint stars than for bright ones. However, I emphasize one important point of the technique employed in this paper. Cluster (or galaxy) memberships are determined simultaneously for stars of very different magnitudes and colors and, given the behavior of the parallax uncertainties as a function of magnitude, the largest weight in determining the distance (and, hence, establishing membership) is given to faint stars with $13 < G < 16$ for most systems. Therefore, stars in the intermediate and bright ranges are anchored with respect to the better characterized faint stars. The reason for not doing a separate analysis for six-parameter solutions at this stage is that the sample of such stars in the intermediate and faint ranges is small (Fig. 12 in L21b) but see below for the value of k .

2.3. What was done with the sample

For the stars in the 26 open clusters, six globular clusters, the LMC, and the SMC I used Eqn. 1 with the Z_{EDR3} from L21b ($Z_{\text{EDR3, Lin}}$) to calculate the group parallaxes and applied Eqn. 2 to obtain $\Delta\varpi_{\text{Lin}}$ for each star. I note that in the case of the LMC and SMC I use the measured group parallax as a reference, not the expected value from external measurements, which is within one sigma of the uncertainty (including the angular covariance terms) but off by a few μas (Paper I). In this way, the analysis in this paper deals with the behavior of Z_{EDR3} as a function of magnitude, color, and ecliptic latitude but does not change the

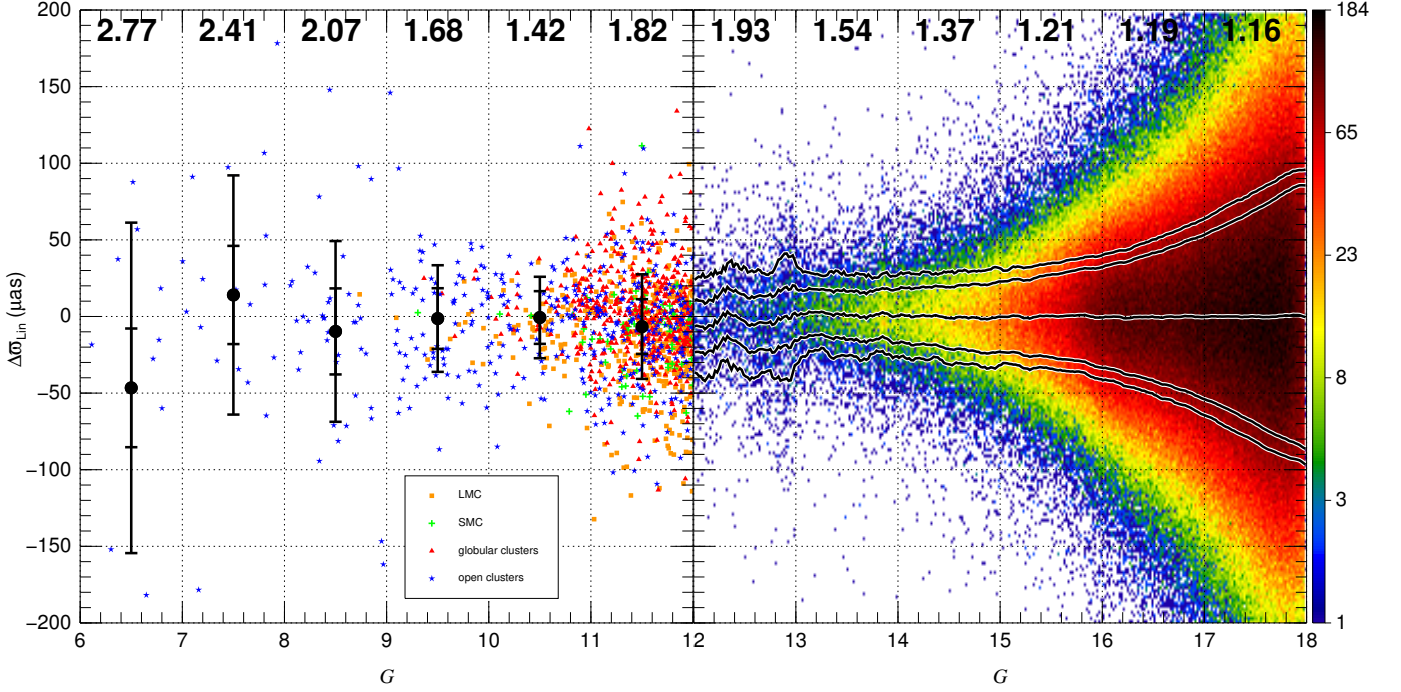


Fig. 4. Residuals using the Lindegren zero point, Δw_{Lin} , as a function of G . The plot is divided into two panels due to the differences in the sample sizes for stars with G between 6 and 12 mag (left panel) and stars with G between 12 and 18 mag (right panel). In the left panel all stars are plotted individually with a color+symbol code used to differentiate between the four samples used in this paper. In the right panel the stellar density is plotted combining all objects and using a logarithmic color scale, with the bar at the left indicating the number of objects in each $0.02 \text{ mag} \times 2 \mu\text{as}$ cell. The black points in the left panel show the average Δw_{Lin} in each magnitude bin. The error bars show the average of the parallax uncertainties (small values) and the dispersion of Δw_{Lin} (large values), also in each magnitude bin. In the right panel the points and error bars are substituted by lines displaying the same information. The text at the top of the panels gives the value of k in each magnitude bin as determined from the dispersion of Δw_{Lin} and the average parallax uncertainty.

global anchoring of the parallaxes with respect to the QSO values or studies the effect of the angular covariance for small or intermediate angles.

As previously mentioned, when normalized by its uncertainty, Δw should have a mean of zero and a standard deviation of one. As discussed in the next section, I detected that is not the case for the combination of Δw_{Lin} and the internal uncertainties: the standard deviation is larger than one for all magnitudes and the mean is very close to one for $G > 13$ but deviates in some cases for brighter stars. The first effect means that k is significantly different from one (even after accounting for the effect of σ_s in Eqn. 3) and the second one that it is possible to improve $Z_{\text{EDR3,Lin}}$ for bright stars. Both of those effects were anticipated in Paper I and are corroborated here. Therefore, after the test using $Z_{\text{EDR3,Lin}}$ I derive and test an alternative zero point in the next section.

3. Results

In this section I first describe the behavior of Δw_{Lin} as a function of magnitude, color, and ecliptic latitude in terms of its average, $\bar{\Delta w}$, and (non-normalized) standard deviation, $\sigma_{\Delta w}$ for the L21b zero point. I then explain how the new zero point is calculated. Finally, I compare the two results.

3.1. The Lindegren zero point

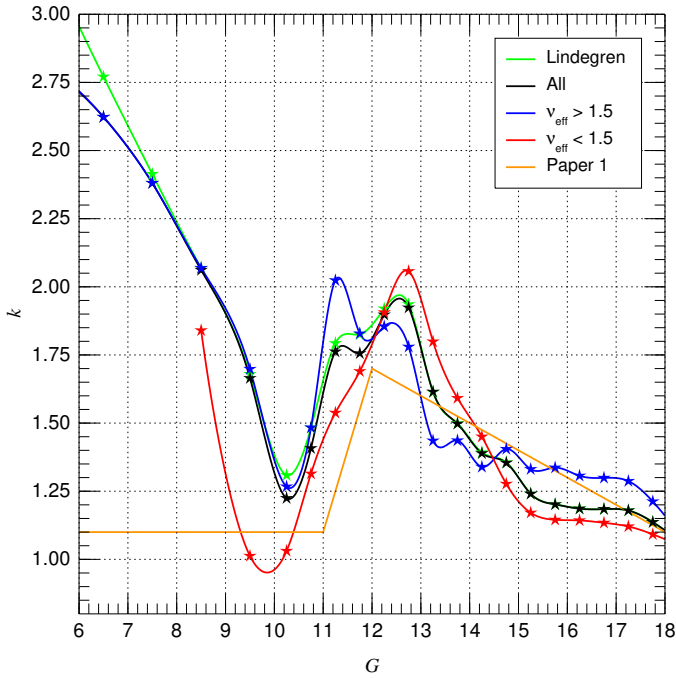
One problem with analyzing data that depends on three parameters (in this case, G , v_{eff} , and β) is how to display them. Given the characteristics of the data, I do it in multiple ways²:

1. Figure 4 plots Δw_{Lin} as a function of G for the whole sample, as that is the parameter that most influences the quality of the parallaxes (to first order, the internal uncertainty is a function of G). In that figure I also show $\bar{\Delta w}$, $\sigma_{\Delta w}$, and the average (internal) parallax uncertainty as a function of G using error bars (left panel) and lines (right panel).
2. The green line in Fig. 5 plots the k value derived from the results plotted in Fig. 4 using Eqn. 3 and assuming that $\sigma_{\Delta w}$ is the external uncertainty.
3. The left panel of Fig. 6 displays a 2-D histogram of $\bar{\Delta w}$ as a function of G and v_{eff} (i.e., a CMD) and in Table 2 the values of a simplified version of the histogram together with the values of $\sigma_{\Delta w}$ and k are given.
4. The inclusion of the effect of the ecliptic latitude is more difficult to visualize because most of the sample is either from the LMC (80.8%), located around the south ecliptic pole, or the SMC (16.3%), not too far from it. On the other hand, the remaining sample (clusters, 2.9%) is more uniformly distributed over the celestial sphere (Fig. 3). Therefore, to compare the effect between a sample that changes little in β with one that is more distributed, I use Figs. 6 and 7, keeping in

² In some cases, the figures/tables show/list the information relevant only to the L21b, others combine it with the equivalent for the zero point in this paper.

Table 2. Statistics (in μas) by G magnitude and v_{eff} ranges using the Lindegren correction. For $G < 9$ the last columns are omitted as only two stars have $v_{\text{eff}} < 1.5 \mu\text{m}^{-1}$.

G	N	all			N	$v_{\text{eff}} > 1.5$			N	$v_{\text{eff}} < 1.5$		
		$\overline{\Delta\varpi}_{\text{Lin}}$	$\sigma_{\Delta\varpi,\text{Lin}}$	k_{Lin}		$\overline{\Delta\varpi}_{\text{Lin}}$	$\sigma_{\Delta\varpi,\text{Lin}}$	k_{Lin}		$\overline{\Delta\varpi}_{\text{Lin}}$	$\sigma_{\Delta\varpi,\text{Lin}}$	k_{Lin}
6.0–7.0	11	−46.58	107.83	2.77	—	—	—	—	—	—	—	—
7.0–8.0	18	+14.03	78.05	2.41	—	—	—	—	—	—	—	—
8.0–9.0	40	−9.75	58.97	2.07	—	—	—	—	—	—	—	—
9.0–10.0	98	−1.35	34.80	1.68	84	−1.82	36.64	1.70	14	+1.45	21.35	1.31
10.0–10.5	154	−3.77	24.30	1.31	113	−5.25	26.06	1.36	41	+0.31	18.28	1.02
10.5–11.0	170	+0.82	27.27	1.48	94	−4.42	28.07	1.54	76	+7.30	24.93	1.33
11.0–11.5	340	−3.48	36.11	1.79	142	−10.24	41.09	2.03	198	+1.36	31.29	1.55
11.5–12.0	637	−8.29	32.93	1.83	242	−16.98	35.42	1.85	395	−2.96	30.13	1.73
12.0–12.5	1098	−2.51	33.16	1.92	394	−3.74	37.77	1.88	704	−1.83	30.29	1.93
12.5–13.0	1768	−2.89	36.84	1.94	758	−4.35	38.58	1.79	1010	−1.79	35.46	2.07
13.0–13.5	2712	+1.95	26.74	1.61	1380	+2.77	25.11	1.44	1332	+1.10	28.31	1.80
13.5–14.0	4877	+0.78	26.36	1.50	2886	+0.42	26.08	1.44	1991	+1.30	26.77	1.59
14.0–14.5	7607	+0.26	28.22	1.39	4060	−1.45	28.11	1.34	3547	+2.22	28.23	1.45
14.5–15.0	14602	−0.95	31.35	1.36	7716	−2.05	33.79	1.41	6886	+0.29	28.32	1.28
15.0–15.5	32994	−0.10	32.73	1.24	11952	−0.26	36.92	1.33	21042	−0.01	30.08	1.17
15.5–16.0	78681	+0.15	37.68	1.20	19235	−0.20	43.98	1.34	59446	+0.27	35.40	1.15
16.0–16.5	146663	−0.49	45.41	1.19	32112	−2.00	52.78	1.31	114551	−0.07	43.11	1.14
16.5–17.0	206874	−0.20	57.49	1.18	54569	−1.25	65.60	1.30	152305	+0.17	54.29	1.13
17.0–17.5	303660	−0.08	73.64	1.18	97619	−0.75	81.98	1.29	206041	+0.24	69.33	1.12
17.5–18.0	373782	+0.20	89.80	1.14	132270	−0.14	96.33	1.21	241512	+0.39	86.01	1.09

**Fig. 5.** k as a function of magnitude for all colors using the Lindegren zero point (Table 2) and for the three cases in Table 5 using the results in this paper. The data points are calculated at 1 mag intervals for $G < 10$ and at 0.5 mag intervals for $G > 10$ and joined by a spline. The orange line shows the approximation derived in Paper 1.

mind Fig. 2 to remember in which areas of the CMD the LMC and SMC population are not dominant.

- To visualize the fitted functions themselves, I use Fig. 8, which is inspired on Fig. 20 of L21b but with two differences: the full functions are plotted (as opposed to individual points) and three panels are used for each fit to show the changes induced by β . In that respect, I note that q_{00} , q_{01} , and

q_{02} shift the different G sections up and down between panels but do not change the overall aspect of the plot. That is caused by q_{11} the mixed color-latitude term and that is why the largest difference between the three left plots in Fig. 8 takes place around $G = 12$, as that is the magnitude at which the q_{11} in $Z_{\text{EDR3,Lin}}$ is larger in the $G = 6 - 18$ range.

I analyze the L21b zero point using the same three magnitude ranges previously described: faint ($13 < G < 18$), intermediate ($9.2 < G < 13$), and bright ($6 < G < 9.2$).

3.1.1. Faint range: $13 < G < 18$

With some minor exceptions, the L21b zero point works very well in the faint magnitude range. $\overline{\Delta\varpi}$ stays close to zero for all magnitudes in Fig. 4 and that is reflected in the first relevant column of Table 2, where all absolute values of $\overline{\Delta\varpi}$ are less than $1 \mu\text{as}$ for $G > 13.5$ and $\sim 2 \mu\text{as}$ in the $G = 13.0 - 13.5$ range. Equivalently, most cells in the left panel of Fig. 6 for $G > 13$. The only significant local effect in Fig. 4 is caused by the concentration of sources around $G = 13.8$ (red clump stars in the relatively metal-rich globular cluster 47 Tuc), but that is just an effect of a few μas . In the left panels of Figs 6 and 7 (especially in the second case), I see a larger effect: for both very blue stars (mostly extreme horizontal branch stars in globular clusters) and very red stars with $G > 16$, $\overline{\Delta\varpi}$ is $< -40 \mu\text{as}$ in Fig. 7 and shows negative values in Fig. 6, with the caveat that the number of stars per cell is small. That is the one of the few CMD regions where the L21b zero point might be improved in the faint range.

3.1.2. Intermediate range: $9.2 < G < 13$

The situation is different in the intermediate range. For $11 < G < 13$, $\overline{\Delta\varpi}$ is consistently negative in Fig. 4 and in the first group of columns in Table 2, with indication of substructures as a function of G at least for $12 < G < 13$ and possibly also for

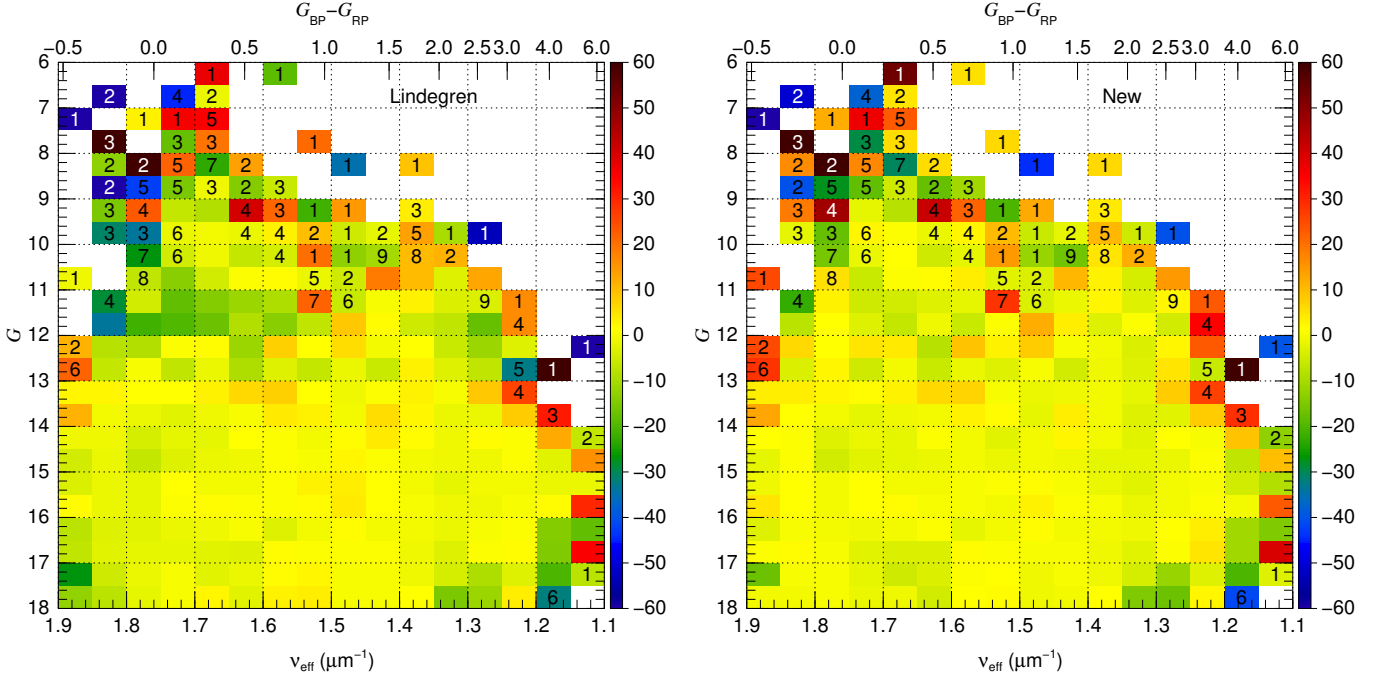


Fig. 6. Average residual as a function of ν_{eff} and G using the Lindgren zero point (left) and the one proposed here (right) for the full sample. The left bar shows the scale in μas . Each cell has a size of $0.05 \mu\text{m}^{-1} \times 0.5 \text{ mag}$. Cells with less than ten objects used to calculate the average include the number of objects. The color scale is capped for values above $60 \mu\text{as}$ or below $-60 \mu\text{as}$ for display purposes but some cells (seven in the left panel, and four in the right panel) are outside that range. The upper x axes use Eqn. 4 of L21a to transform from ν_{eff} to $G_{\text{BP}} - G_{\text{RP}}$.

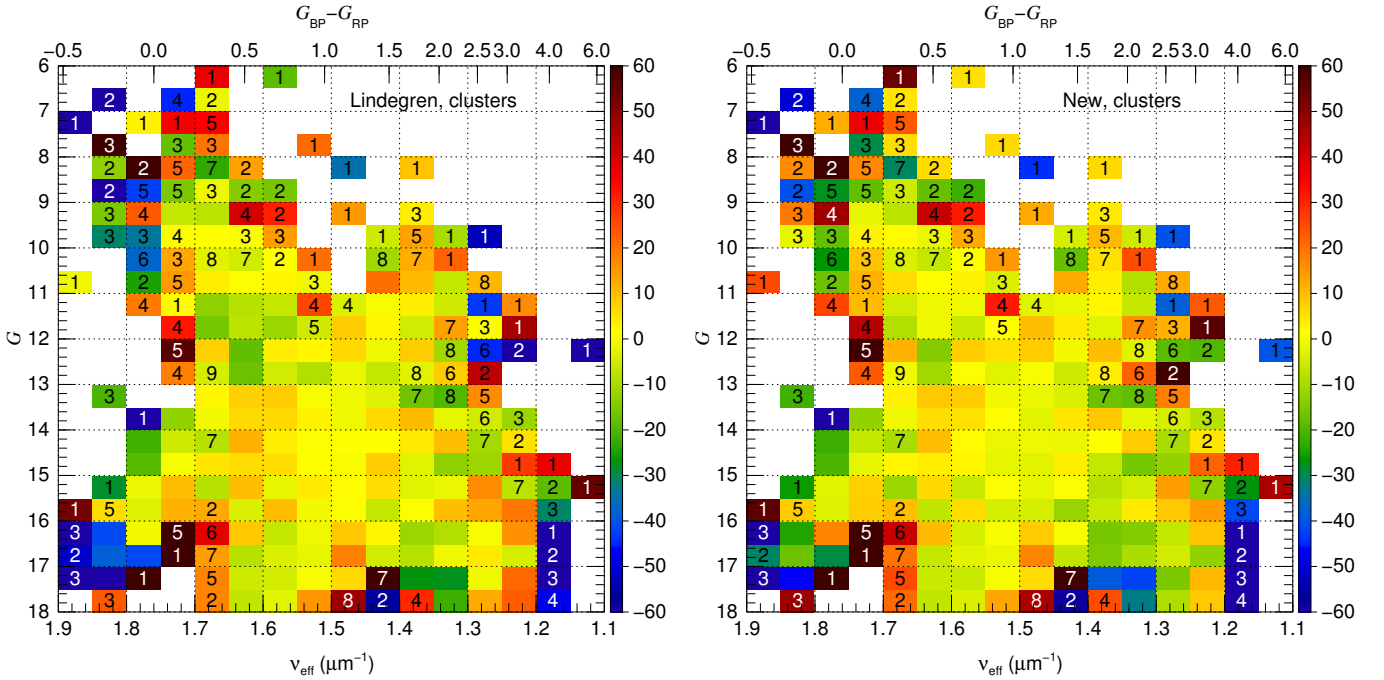


Fig. 7. Same as Fig. 6, but using only the cluster sample. Here the number of cells outside the range is 17 in the left panel and 16 in the right panel.

$11 < G < 12$. The two additional $\overline{\Delta\varpi}$ columns in Table 2 and the left panel of Fig. 6 reveal that the deviations are significantly larger for blue stars, with a value of almost $-17 \mu\text{as}$ for the 242 stars with $11.5 < G < 12.0$ and $\nu_{\text{eff}} > 1.5 \mu\text{m}^{-1}$. This effect was already hinted at by L21b (their subsection 6.2) in the LMC data but could not be better checked by them due to the absence of a larger sample. For $9.2 < G < 11$, $\overline{\Delta\varpi}$ is also negative for blue stars (but by a smaller amount than for $11 < G < 12$) but for red

stars it is positive (with a smaller sample). Therefore, the L21b zero point can be significantly improved in this range.

3.1.3. Bright range: $6 < G < 9.2$

In this range the number of stars is smaller, so the analysis of the L21b zero point cannot be as thorough. Two main issues can be described. First, $\sigma_{\Delta\varpi}$ increases significantly, with a large ef-

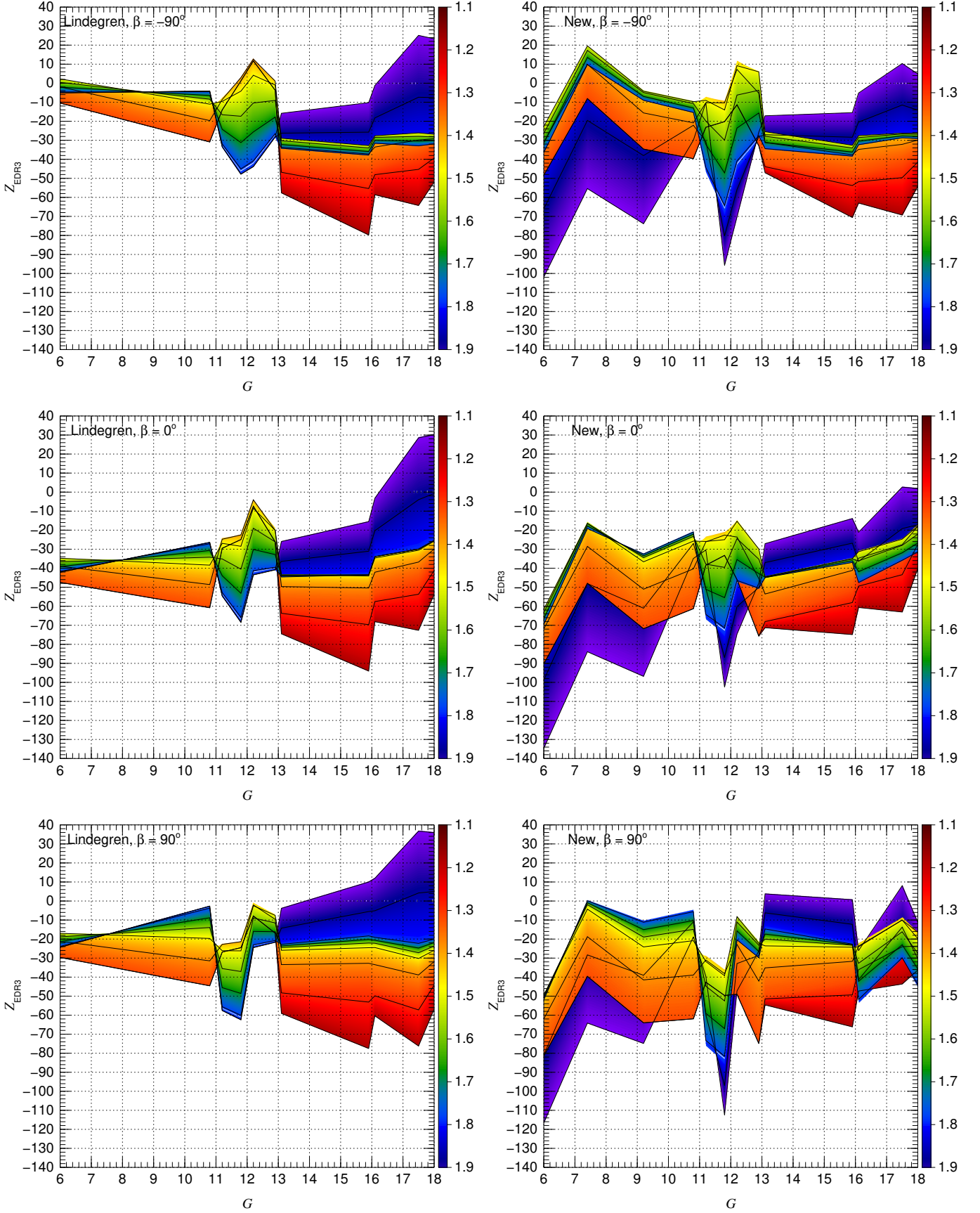


Fig. 8. Z_{EDR3} as a function of G (horizontal axes) and ν_{eff} (color bar) for the L21b zero point (left column) and the new zero point in this paper (right column). The black lines correspond to the values of the nine ticks in the color bar. To visualize the β effect, each Z_{EDR3} is evaluated at the ecliptic south pole (top panels), equator (middle panels), and north pole (bottom panels). I note that for $G < 12.9$ Z_{EDR3} has no color dependence in the $\nu_{\text{eff}} = 1.1 - 1.24 \mu\text{m}^{-1}$ range, as $q_{30} = 0$. Compare with the top panel in Fig. 20 of L21b.

fect on k (see below). Second, $\overline{\Delta\varpi}$ has the largest deviations from zero of all ranges, following a sequence of negative-positive-negative values as one progresses toward brighter magnitudes. However, those aspects have to be qualified by the small sample and by almost all bright stars in the sample being blue. It is possible to improve the L21b zero point in this range but being subject to larger uncertainties in the outcome.

3.1.4. The k multiplicative constant

The behavior of k in Fig. 5 for L21b has a qualitative similar one to the approximation derived in Paper I for $G > 10$. An increase from ~ 1.1 at $G = 18$ as we move toward $G \sim 12$ followed by a decrease as we move toward $G = 10$. However, some (relatively small) differences are seen in that range, not surprising given the better sampling of the data here: the peak around $G \sim 12$ is taller, wider, and has some structure. The situation is very different for $G < 10$, a range that was not probed in Paper I. Starting around $G = 10$, where $k \sim 1.3$, it grows to values close to 2.0 around $G = 9$ and close to 3.0 for the brightest stars sampled here. Pending the derivation of the new zero point below, I defer until then the analysis of the consequences of this effect.

3.2. Calculating the new zero point

As just described, the Lindegren zero point works reasonably well for most values of its parameters, G , v_{eff} , and β , but can be tweaked in some circumstances. Based on that, I define the new zero point as the sum of the Lindegren one and a correction term:

$$Z_{\text{EDR3,new}} = Z_{\text{EDR3,Lin}} + \Delta Z_{\text{EDR3}}. \quad (5)$$

The goal is to derive the optimal ΔZ_{EDR3} by fitting $\Delta\varpi_{\text{Lin}}$ to obtain $Z_{\text{EDR3,new}}$. This strategy works because the zero point is the sum of a series of linear terms. The decomposition into two terms has several advantages. First, it allows us to characterize the impact of the correction better. Second, I can fit just a selection of the whole set of coefficients, leaving the ones from L21b that do not require changes to be left in place. And third, it allows the anchoring of the parallaxes to remain unchanged, as previously mentioned.

To calculate ΔZ_{EDR3} I assumed the same functional form as L21b and added three magnitude breakpoints (knots) at $G = 7.4, 9.2$, and 18.0 . The last one is added because it is the end of the magnitude range in our sample. The first two are added based on Fig. 4, as the behavior of $\Delta\varpi$ in G there is not linear in the $G = 6.0$ - 10.8 range and those are the apparent magnitudes at which the behavior changes (but see below for the restrictions placed on the fitted coefficients in that range).

To fit ΔZ_{EDR3} I wrote a program in IDL based on the MPFIT package (Markwardt 2009)³. MPFIT allows for arbitrary functions to be fitted to almost any type of data while fixing the value of some coefficients and tying up others among them. As L21b correctly cautions, it is important to avoid overfitting. Therefore, initially I only fitted the coefficients where enough data were present and, by trial and error, I added additional restrictions. In the end, the following coefficients for ΔZ_{EDR3} were fit:

- For the three breakpoints at $G = 6.0, 7.4$, and 9.2 , only q_{00} was fit at each one of them. q_{30} was not fit (as there are no stars as red as needed, see below) and the rest of the coefficients were tied up, that is, forced to have the same values at

the three breakpoints. For q_{11} the range of bright magnitudes where the coefficients are tied up was extended to $G = 10.8$ and for q_{20} to $G = 10.8, 11.2$, and 11.8 .

- The mixed latitude-color term, q_{11} , was also tied up in three additional regions: (a) $G = 11.2$ and 11.8 , (b) $G = 12.2$ and 12.9 , and (c) $G = 16.1, 17.5$, and 18.0 .
- The cubic term for red stars, q_{20} was tied up for G at 17.5 and 18.0 .
- As there are few very red stars in the sample, q_{30} was only fit in the $G = 13.1$ - 17.5 range and even there, the two values at 13.1 and 15.9 were tied up and the same was done for the two values at 16.1 and 17.5 .

The fitted coefficients for ΔZ_{EDR3} are given in Table 3. The last two columns give the combinations of the first five coefficients at the south ecliptic pole, which is a reasonable approximation for the LMC stars. The final $Z_{\text{EDR3,new}}$ is given in Table 4, where for magnitudes fainter than $G = 18.0$ the values given are simply those of $Z_{\text{EDR3,Lin}}$, as the sample in this paper does not reach those very faint magnitudes. The values of the new zero point are plotted in the right column of Fig. 8, allowing for a direct comparison with the L21b zero point. To facilitate the implementation of the new results, two IDL routines are given in Tables A.1 and A.2. The first one produces the k multiplicative constant and the second one the new zero point.

As a final note, I am fitting $\Delta\varpi_{\text{Lin}}$ to obtain a new ΔZ_{EDR3} and the values of $\Delta\varpi_{\text{Lin}}$ depend on the group parallaxes calculated with the L21b zero point. In principle, one could iterate the process by using the new group parallaxes obtained with $Z_{\text{EDR3,new}}$ (i.e., the ones that are listed in Villafranca II for the open clusters) and calculate a new incremental zero point to be added to the previous one. However, that was found unnecessary because the differences between the old and new group parallaxes are small ($\sim 1 \mu\text{as}$) and unbiased (some positive and some negative), leading to very similar values of $Z_{\text{EDR3,new}}$.

3.3. Analysis

I now analyze $Z_{\text{EDR3,new}}$ by using it to calculate the new group parallaxes and studying the residuals using the new zero point, $\Delta\varpi_{\text{new}}$. For that purpose I use Fig. 9, the equivalent to Fig. 4, Table 5, the equivalent to Table 2, and the already introduced Figs. 5, 6, 7, and 8 and Tables 3 and 4. As I did for the Lindegren zero point, I divide the analysis in the same three magnitude ranges.

3.3.1. Faint range: $13 < G < 18$

As expected, the differences between the Lindegren and the new zero points are small for most values of the parameter space for faint stars. This is especially true near the south ecliptic pole (in our sample, the LMC and SMC), as evidenced by the small values in the last two columns of Table 3 and the similar appearance of the top two panels in Fig. 8 for $G > 13$. However, in some cases the differences are significant:

- The largest one is the existence of a relatively large ΔZ_{EDR3} mixed color-latitude term (q_{11}) for $G > 16.1$. While the top two plots of Fig. 8 are similar for those magnitudes, the bottom two plots are quite different.
- The new zero point also has a significant q_{40} term (blue stars) in this magnitude range, as established with the help of extreme horizontal branch stars in globular clusters. $\Delta\varpi_{\text{new}}$ is smaller than $\Delta\varpi_{\text{Lin}}$ for them (bottom left corner of both panels in Fig. 7, the effect is also seen to some degree in Fig. 6).

³ Available from <http://pur1.com/net/mpfit>.

Table 3. $\Delta Z_{\text{EDR3}}(G, \nu_{\text{eff}}, \beta)$ coefficients for 5-parameter solutions calculated in this paper. The last two columns show the combinations of the first five coefficients evaluated at the south ecliptic pole.

G	q_{00}	q_{01}	q_{02}	q_{10}	q_{11}	q_{20}	q_{30}	q_{40}	$q_{00} - q_{01} + \frac{2}{3}q_{02}$	$q_{10} - q_{11}$
6.0	-27.35	-2.35	-2.01	-5.9	+19.1	-1272	—	-358.1	-26.34	-25.0
7.4	+18.88	-2.35	-2.01	-5.9	+19.1	-1272	—	-358.1	+19.89	-25.0
9.2	+0.04	-2.35	-2.01	-5.9	+19.1	-1272	—	-358.1	+1.05	-25.0
10.8	+7.20	+0.29	-12.56	-23.7	+19.1	-1272	—	-78.6	-1.46	-42.8
11.2	-3.05	-2.98	-3.57	-43.9	+1.6	-1272	—	+203.1	-2.45	-45.5
11.8	-3.41	-1.47	-14.93	-32.0	+1.6	-1272	—	-155.3	-11.89	-33.6
12.2	-3.34	-3.60	+6.46	+1.5	+22.6	-2368	—	-144.2	+4.57	-21.1
12.9	-6.96	-8.99	+5.91	-9.2	+22.6	-3096	—	+23.6	+5.97	-31.8
13.1	+0.48	+0.70	+4.27	+2.8	+15.6	-418	-75.8	-4.8	+2.63	-12.8
15.9	+5.51	-0.46	-8.92	-9.1	-6.5	-152	-75.8	-25.9	+0.02	-2.6
16.1	-2.13	-4.14	-3.11	-56.8	-53.6	-301	+6.6	-17.6	-0.06	-3.2
17.5	+4.16	+5.92	+4.16	-39.2	-53.6	-119	+6.6	-107.0	+1.01	+14.4
18.0	+2.71	-1.53	-4.55	-46.5	-53.6	-119	—	-118.7	+1.21	+7.1

Table 4. $Z_{\text{EDR3,new}}(G, \nu_{\text{eff}}, \beta)$ coefficients for 5-parameter solutions calculated from L21b and the results in this paper.

G	q_{00}	q_{01}	q_{02}	q_{10}	q_{11}	q_{20}	q_{30}	q_{40}
6.0	-54.33	-11.97	+25.39	-31.0	+19.1	-2529	—	-358.1
7.4	-8.17	-10.06	+24.12	-13.4	+23.7	-2529	—	-358.1
9.2	-27.11	-7.60	+22.48	+9.3	+29.6	-2529	—	-358.1
10.8	-20.03	-2.78	+10.48	+11.6	+34.8	-2529	—	-78.6
11.2	-33.38	-12.21	+5.51	-132.3	-10.2	-2529	—	+203.1
11.8	-36.95	-11.55	-1.65	-158.7	+13.2	-2529	—	-155.3
12.2	-16.99	-3.67	+15.81	-109.9	+63.2	-3625	—	-144.2
12.9	-26.49	-10.63	+21.77	-76.0	+43.2	-4353	—	+23.6
13.1	-37.51	+3.33	+20.41	-2.9	+29.6	-1675	+32.1	+99.5
15.9	-32.82	+5.15	+6.50	-9.1	+12.2	-1341	+168.0	+129.3
16.1	-33.18	-1.31	+5.48	-56.8	-38.1	-1705	+112.1	+153.1
17.5	-25.02	+5.83	+6.57	-39.2	-29.1	-1284	+196.3	+218.0
18.0	-22.88	+0.40	-5.10	-46.5	-35.4	-896	+126.5	+190.2
19.0	-18.40	+5.98	-6.46	—	+5.5	—	—	+276.6
20.0	-12.65	-4.57	-7.46	—	+97.9	—	—	—
21.0	-18.22	-15.24	-18.54	—	+128.2	—	—	—

Table 5. Statistics (in μas) by G magnitude and ν_{eff} ranges using the results in this paper.

G	N	all			N	$\nu_{\text{eff}} > 1.5$			N	$\nu_{\text{eff}} < 1.5$		
		$\overline{\Delta\varpi}_{\text{new}}$	$\sigma_{\Delta\varpi,\text{new}}$	k_{new}		$\overline{\Delta\varpi}_{\text{new}}$	$\sigma_{\Delta\varpi,\text{new}}$	k_{new}		$\overline{\Delta\varpi}_{\text{new}}$	$\sigma_{\Delta\varpi,\text{new}}$	k_{new}
6.0- 7.0	11	-26.01	102.14	2.62	—	—	—	—	—	—	—	—
7.0- 8.0	18	+11.76	77.00	2.38	—	—	—	—	—	—	—	—
8.0- 9.0	40	-7.72	58.77	2.06	—	—	—	—	—	—	—	—
9.0-10.0	98	+3.41	34.52	1.66	84	+3.72	36.64	1.70	14	+1.53	17.79	1.01
10.0-10.5	154	-2.14	23.02	1.22	113	-1.31	24.51	1.27	41	-4.43	18.39	1.03
10.5-11.0	170	+1.80	26.08	1.41	94	+0.48	27.20	1.48	76	+3.43	24.71	1.31
11.0-11.5	340	+0.07	35.55	1.76	142	-1.49	41.03	2.02	198	+1.19	31.09	1.54
11.5-12.0	637	-0.17	31.79	1.76	242	-2.68	35.03	1.83	395	+1.37	29.58	1.69
12.0-12.5	1098	+1.27	32.82	1.90	394	+2.57	37.36	1.85	704	+0.55	29.98	1.91
12.5-13.0	1768	-1.92	36.63	1.92	758	-2.13	38.39	1.78	1010	-1.77	35.26	2.06
13.0-13.5	2712	+1.31	26.76	1.61	1380	+3.29	25.11	1.44	1332	-0.73	28.23	1.80
13.5-14.0	4877	+0.05	26.34	1.50	2886	+0.62	26.05	1.44	1991	-0.78	26.75	1.59
14.0-14.5	7607	-0.28	28.17	1.39	4060	-0.77	28.10	1.34	3547	+0.27	28.23	1.45
14.5-15.0	14 602	-1.37	31.31	1.35	7716	-1.56	33.76	1.40	6886	-1.16	28.32	1.28
15.0-15.5	32 994	-0.22	32.70	1.24	11 952	+0.53	36.87	1.33	21 042	-0.64	30.08	1.17
15.5-16.0	78 681	+0.15	37.67	1.20	19 235	+0.71	43.98	1.34	59 446	-0.04	35.38	1.15
16.0-16.5	146 663	-0.06	45.40	1.19	32 112	-0.15	52.77	1.31	114 551	-0.04	43.11	1.14
16.5-17.0	206 874	+0.17	57.48	1.18	54 569	+0.38	65.58	1.30	152 305	+0.09	54.29	1.13
17.0-17.5	303 660	+0.01	73.62	1.18	97 619	+0.16	81.93	1.29	206 041	-0.06	69.34	1.12
17.5-18.0	373 782	-0.09	89.77	1.14	132 270	+0.54	96.27	1.21	241 512	-0.44	86.00	1.09

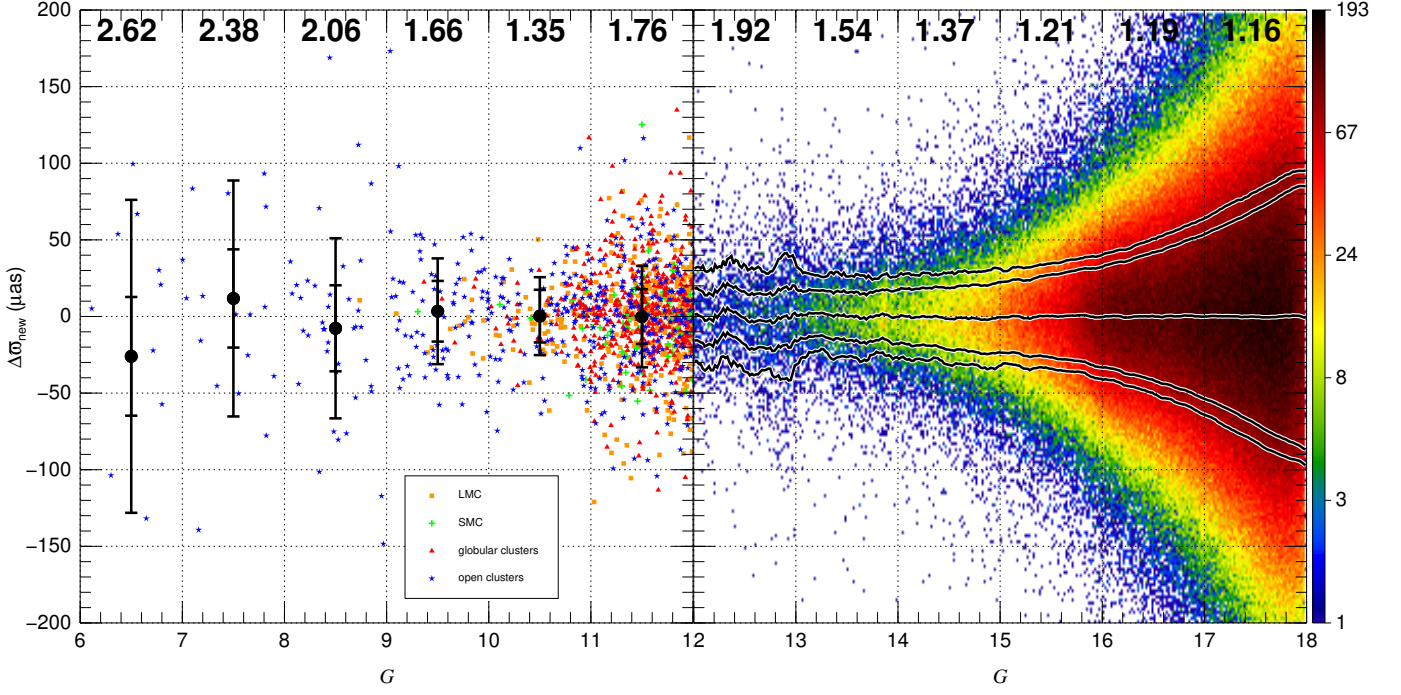


Fig. 9. Same as Fig. 4, but using the zero point proposed here.

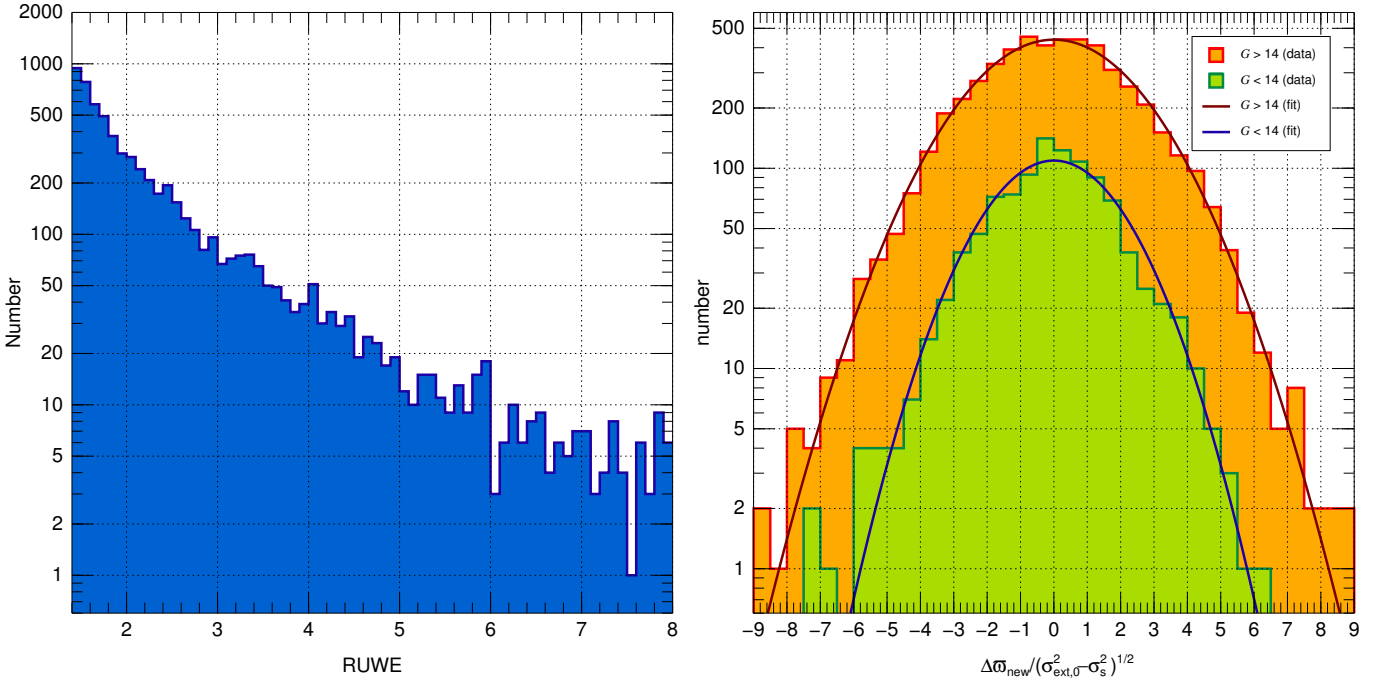


Fig. 10. (left) RUWE histogram of five-parameter sources from the 32 stellar clusters in our sample used to evaluate k_{ext} . (right) Normalized parallax histograms for faint and bright sources with RUWE between 1.4 and 8.0. The two fits correspond to values of k_{ext} of 2.36 and 1.88, respectively.

However, some residuals are still seen, especially for stars bluer than $\nu_{\text{eff}} = 1.8 \mu\text{m}^{-1}$. At this stage it is not clear whether the effect is caused by small number statistics or by the need of using a different functional form for the zero point (e.g., a q_{41} term), but I note that the effect is also seen in the bottom two panels of Fig. 10 in L21b.

- L21b detected the existence of a “hook” in the behavior of the reddest stars ($\nu_{\text{eff}} < 1.18 \mu\text{m}^{-1}$) for $G > 16$. The effect is also seen in the bottom right corners of Figs. 6 and 7 but

as the functional form does not include a term there, the new zero point does not correct for it and the appearance does not change significantly between the left and right panels.

Nevertheless, we should bear in mind that for most stars in this magnitude range the effect is small. In that way, Figs 4 and 9 are very similar for $G > 13$. Doing a more quantitative comparison, nine out of the thirty values of $\overline{\Delta\pi}$ in Table 2 have absolute values larger than $1 \mu\text{as}$, a number that in Table 5 is reduced to

five (very good statistics if one bears in mind that $\sigma_s = 10.3 \mu\text{as}$). In summary, for $13 < G < 16$ the new zero point is very similar to the Lindegren zero point and for $16 < G < 18$ some differences appear for stars far from the south ecliptic pole and for very blue and very red stars.

3.3.2. Intermediate range: $9.2 < G < 13$

The new zero point is significantly different from the Lindegren one for intermediate magnitudes, even for positions close to the south ecliptic pole (Fig. 8). For $\beta = -90^\circ$, $Z_{\text{EDR3,new}}$ is qualitatively similar to $Z_{\text{EDR3,Lin}}$ (with a reversal of the behavior as a function of color with respect to fainter magnitudes in both cases) but quantitatively different for $11 < G < 13$. For brighter stars (continuing to $G = 6$) a large q_{40} term appears, making $Z_{\text{EDR3,new}}$ more negative for blue stars. As for the changes as a function of β , they are small for $11 < G < 12$ and significant otherwise.

Analyzing the $\overline{\Delta\varpi}$ values in Table 2 for $9 < G < 13$ I find just six out of twenty one with absolute values smaller than $2 \mu\text{as}$ and five with absolute values larger than $5 \mu\text{as}$. On the other hand, in Table 5 thirteen out of twenty one values have absolute values smaller than $2 \mu\text{as}$ and there are none above $5 \mu\text{as}$. It is clear that the new zero point lowers the residuals and provides a better fit. The effect is also seen in the comparison between Figs 4 and 9, especially for $11 < G < 13$. I note the apparent existence of some fine structure as a function of G with an amplitude of a few μas for at least $12 < G < 13$ that could be further corrected in the future by introducing additional magnitude breakpoints.

The improvement is not the same for all magnitudes and colors. From Tables 2 and 5 and Figs. 6 and 7, we see that it is larger for blue stars than for red ones and for $11 < G < 12$ than for other magnitudes in this range. The main shortcoming of the new zero point arises from the relatively small sample size, especially for the brighter part of the magnitude range for red stars. One possible improvement in this sense would be to add open clusters with red supergiants to the analysis. In summary, for $9.2 < G < 13$ the new zero point provides a significant improvement with respect to the Lindegren zero point.

3.3.3. Bright range: $6 < G < 9.2$

Once we get to this magnitude range, the sample is highly incomplete and consists almost exclusively of blue stars. ΔZ_{EDR3} has large q_{00} and (as already mentioned) q_{40} terms, leading to significant changes in the overall zero point and on its color dependence for blue stars (Fig. 8). $Z_{\text{EDR3,new}}$ is capable of partially flattening the behavior of $\overline{\Delta\varpi}$ in Fig. 9 and Table 5 with respect to Fig. 4 and Table 2. Still, the values are not zero and the most visible characteristic is the persistence of the large values of $\sigma_{\Delta\varpi}$, which in turn lead to the same effect for k , as we see in the next subsection. In summary, for bright stars the new zero point improves upon the Lindegren zero point but provides little information for red stars and this magnitude range is dominated by the effect of the large dispersion of the results, indicating a significant underestimation of the external parallax uncertainties by the internal values.

3.3.4. The k multiplicative constant

Table 5 lists the values of k as a function of magnitude using the new zero point, including all colors in the calculation or just the blue or the red stars. The values are also plotted in Fig. 5

G	N	k_{ext}
6-13	276	1.50
13-14	759	2.01
14-15	1050	2.28
15-16	1212	2.38
16-17	1230	2.44
17-18	1700	2.32

Table 6. k_{ext} calculated in magnitude bins for five-parameter solutions using the stellar cluster data for objects with RUWE between 1.4 and 8.0. The second column gives the number of objects per bin.

and can be compared with the results from the Lindegren zero point in Table 2 and in the same figure. For faint stars the results for both zero points are identical, an indication of the similarity between the two zero points in that magnitude range. For intermediate and bright stars the new zero point reduces the value of k but only slightly so. This must be interpreted as the effect of ΔZ_{EDR3} , the transformation from the Lindegren zero point to the new one (the correction of a systematic effect), being in general small compared to the true random uncertainties. The ultimate reason why we can measure ΔZ_{EDR3} is because we are using large numbers of stars in each cluster or galaxy. On the other hand, the introduction of the k value (and, to a lesser extent, of σ_s) in the transformation of internal uncertainties to external ones is an important effect, given that it is significantly larger than one.

The comparison between blue and red stars in Table 5 shows a similar behavior as a function of G , indicating that a single $k(G)$ is a good approximation. Nevertheless, there are some differences. For most magnitudes k appears to be slightly lower for red stars. The exception is the region around $G \approx 12.7$, where the local maximum in k for red stars is located. The equivalent maximum for blue stars is located around $G \approx 11.3$.

The largest values of k occur for bright stars ($G < 9.2$) and that is the single most important conclusion of this work: using the internal uncertainties leads to a significant underestimation of their *Gaia* EDR3 distance uncertainties. The effect is also important for stars with $11 < G < 13$. An example of the effect is seen in the case of the eleven intermediate/bright stars listed in Table 1: all of their *Gaia* EDR3 parallaxes are within 3 sigmas of the group values if one uses the $k(G)$ in Table 5.

3.3.5. Objects with large RUWE

The results presented so far refer to objects with five-parameter solutions and “good” RUWE, that is, values up to 1.4. However, as shown in Paper I, it is possible to treat objects with RUWE larger than 1.4 by introducing an additional factor, k_{ext} , in Eqn. 3 multiplying σ_{int} , that is:

$$\sigma_{\text{ext}} = \begin{cases} \sqrt{k^2 \sigma_{\text{int}}^2 + \sigma_s^2}, & \text{RUWE} < 1.4 \\ \sqrt{k_{\text{ext}}^2 k^2 \sigma_{\text{int}}^2 + \sigma_s^2}, & \text{RUWE} > 1.4. \end{cases} \quad (6)$$

Here I present an extended analysis of this issue.

I select the five-parameter solutions in each of the 32 clusters in our sample with [a] G between 6 and 18, [b] RUWE between 1.4 and 8.0, [c] no restrictions on parallax uncertainty, and [d] the rest of the restrictions that apply to each individual cluster. I apply $Z_{\text{EDR3,new}}$ and subtract the group parallax to each individual parallax value to calculate $\Delta\varpi_{\text{new}}$ and I use Eqn. 3 to obtain

$\sigma_{\text{ext},0}$, that is, the external uncertainty assuming the same k as for objects with RUWE lower than 1.4. Finally, I make a 9-sigma cut in normalized parallax, the value being so high because we expect the real external uncertainties to be larger than for objects with good RUWE. The final sample has 6227 objects.

The distributions of RUWE and of normalized $\Delta\varpi_{\text{new}}$ are shown in Fig. 10. I divide the sample in a faint and a bright range (limited by $G = 14$) and calculate Gaussian fits with zero mean. The results are excellent, indicating that parallaxes with large RUWE are not strongly biased toward higher or lower values and that the inclusion of a k_{ext} results in external uncertainties with the proper behavior. k_{ext} is significantly larger for fainter stars, leading us to divide G in bins to tabulate its behavior. Unfortunately, there are few bright stars in this sample, so the information there is limited and a single bin for the $G = 6-13$ has to be used. The results are given in Table 3.3.5 and have been incorporated into Table A.1.

3.3.6. Objects with six-parameter astrometric solutions

As previously mentioned, there are not enough stars with six-parameter solutions to derive a new Z_{EDR3} for them. However, as we have seen, the value of k is relatively robust with respect to the zero point and can be calculated even with a relatively small number of points. In the case of our cluster sample, we have enough stars to determine it for the range $13 < G < 18$. The values of k for six-parameter solutions there follow the same pattern as in Fig. 5 for five-parameter solutions, growing from $G \sim 18$ to $G \sim 13$ but with values that are ~ 1.25 times higher. Therefore, a simple approximation is to use a value of k_{ext} of 1.25 for six-parameter solutions, that is:

$$\sigma_{\text{ext}} = \sqrt{1.25^2 k^2 \sigma_{\text{int}}^2 + \sigma_s^2} \text{ for six-parameter solutions} \quad (7)$$

but I note that it is not tested for $G < 13$. That approximation has been incorporated into Table A.1.

4. Summary and future work

In this paper I have presented a new zero point for *Gaia* EDR3 parallaxes as a function of magnitude, color, and ecliptic latitude. I have used the same functional form as L21b (Eqn. 4) but derived the zero point using a combination of data from the LMC, the SMC, globular clusters, and open clusters. The differences between the two zero points are small for faint stars ($G > 13$) but become significant for stars brighter than that, though it should be noted that for $G < 9.2$ the zero point is poorly defined due to the small size of the sample. As a second result, I have determined that the multiplicative constant k that is used to convert from internal parallax uncertainties to external ones (Eqn. 3) is significantly larger than one for most stars and even larger than two for $G < 9.2$. k is found to be even larger for objects with RUWE larger than 1.4 or with six-parameter solutions. Therefore, the distance uncertainties derived assuming internal parallax uncertainties will be, in general, underestimated.

Gaia DR4 is still several years in the future and this paper has not exploited all of the possibilities for improving on the zero point. The most obvious future line of work would be adding more clusters to improve the statistics for bright stars. It would be especially interesting to include young clusters with red supergiants, as those would extend the sampling to a larger range of colors (bright red stars) and of ecliptic latitudes. Red giants

in additional globular clusters would also help but to a lesser degree regarding bright red stars, given that the tip of the red giant branch (TRGB) is not too bright (bottom left panel in Fig. 2) and that there are only a few nearby globular clusters. However, adding globular clusters would be helpful in calibrating two regions of the CMD: RGB stars for the intermediate/faint very red region (the dominant *Gaia* population in some regions of the Galactic plane lies there in the form of high-extinction red giants) and blue horizontal branch (BHB) stars for the faint very blue region. The latter could be used to test whether the residuals for very blue stars described in subsection 3.3.1 could be corrected with a latitude dependence. Other possibilities would be testing new basis functions and magnitude breakpoints and building a sample large enough to test the zero point for six-parameter solutions. Once *Gaia* DR4 becomes available, these same clusters could be used to determine its (hopefully smaller) parallax zero points.

Acknowledgements. I acknowledge support from the Spanish Government Ministerio de Ciencia through grant PGC2018-95 049-B-C22. This work has made use of data from the European Space Agency (ESA) mission *Gaia*⁴, processed by the *Gaia* Data Processing and Analysis Consortium (DPAC⁵). Funding for the DPAC has been provided by national institutions, in particular the institutions participating in the *Gaia* Multilateral Agreement. The *Gaia* data is processed with the computer resources at Mare Nostrum and the technical support provided by BSC-CNS.

References

- Brown, A. G. A., Vallenari, A., Prusti, T., et al. 2021, A&A, 649, A1
- Campillay, A. R., Arias, J. I., Barbá, R. H., et al. 2019, MNRAS, 484, 2137
- Lindgren, L., Klioner, S. A., Hernández, J., et al. 2021a, A&A, 649, A2
- Lindgren, L., Bastian, U., Biermann, M., et al. 2021b, A&A, 649, A4
- Luri, X., Chemin, L., Clementini, G., et al. 2021, A&A, 649, A7
- Maíz Apellániz, J. 2019, A&A, 630, A119
- Maíz Apellániz, J., Barbá, R. H., Fernández Aranda, R., et al. 2021a, arXiv e-prints, arXiv:2110.01464 (Villafranca II, accepted in A&A)
- Maíz Apellániz, J., Crespo Bellido, P., Barbá, R. H., Fernández Aranda, R., & Sota, A. 2020, A&A, 643, A138 (Villafranca I)
- Maíz Apellániz, J., Pantaleoni González, M., & Barbá, R. H. 2021b, A&A, 649, A13 (Paper I)
- Markwardt, C. B. 2009, in Astronomical Society of the Pacific Conference Series, Vol. 411, Astronomical Data Analysis Software and Systems XVIII, ed. D. A. Bohlender, D. Durand, & P. Dowler, 251

⁴ <https://www.cosmos.esa.int/gaia>

⁵ <https://www.cosmos.esa.int/web/gaia/dpac/consortium>

Appendix A: IDL codes

Table A.1. Function that calculates *Gaia* EDR3 parallax external uncertainties.

```
FUNCTION SPICOR, spi, gmag, ruwe, npar  
; ; ; ; ;  
; This function returns the parallax external uncertainties for Gaia  
; EDR3 in milliarcseconds for an array of values. spi, gmag, ruwe,  
; and npar must be arrays with the same number of elements.  
; ; ; ; ;  
; Positional parameters:  
; spi:      Gaia EDR3 parallax uncertainty in milliarcseconds.  
; gmag:     Gaia EDR3 G magnitude (original, not corrected).  
; ruwe:     Gaia EDR3 RUWE.  
; npar:     Gaia EDR3 number of parameters of the solution (5 or 6).  
; ; ; ; ;  
gref = [ 6.50, 7.50, 8.50, 9.50, 10.25, 10.75, 11.25, 11.75, 12.25, 12.75, $  
        13.25, 13.75, 14.25, 14.75, 15.25, 15.75, 16.25, 16.75, 17.25, 17.75] $  
kref = [ 2.62, 2.38, 2.06, 1.66, 1.22, 1.41, 1.76, 1.76, 1.90, 1.92, $  
        1.61, 1.50, 1.39, 1.35, 1.24, 1.20, 1.19, 1.18, 1.18, 1.14]  
k = INTERPOL(kref, gref, >gmag<18, /SPLINE)  
geref = [ 6.00, 12.50, 13.50, 14.50, 15.50, 16.50, 17.50]  
keref = [ 0.50, 0.50, 1.01, 1.28, 1.38, 1.44, 1.32]  
k = k*(1 + $  
    (INTERPOL(keref, geref, >gmag<18, /SPLINE) > 0.5))*(ruwe GT 1.4))  
k = k*(1 + 0.25*npar EQ 6.)  
out = SQRT((spi*k)^2 + 0.0103^2)  
RETURN, out  
END
```

Table A.2. Function that calculates the *Gaia* EDR3 zero point for an array of values.

```

FUNCTION ZPEDR3, gmag, nueff, lat, npar, ORIG=orig
;
; This function returns the parallax zero point correction for Gaia EDR3 in
; microarcseconds for an array of values. gmag, nueff, lat, and npar must
; be arrays with the same number of elements. By default, it applies the
; new zero point. The code uses VALID_NUM in the IDL astronomy library:
; https://idlastro.gsfc.nasa.gov/ftp/pro/misc/valid_num.pro
;
; Positional parameters:
; gmag: Gaia EDR3 G magnitude (original, not corrected).
; nueff: Effective wavenumber, real for five-parameter solutions and
; pseudocolor for six-parameter solutions, in inverse microns.
; lat: Ecliptic latitude in degrees.
; npar: Number of parameters of the solution (2, 5, or 6).
;
; Keyword parameters:
; ORIG: Flag to use the Lindegren correction instead of the new one.
;
;
IF NOT KEYWORD_SET(ORIG) THEN BEGIN ; New
  gcut5 = [ 6.0, 7.4, 9.2, 10.8, 11.2, 11.8, 12.2, 12.9, 13.1, 15.9, 16.1, 17.5, 18.0, 19.0, 20.0, 21.0 ]
  q500 = [ -54.33, -8.17, -27.11, -20.03, -33.38, -36.95, -16.99, -26.49, -37.51, -32.82, -33.18, -25.02, -22.88, -18.40, -12.65, -18.22 ]
  q501 = [ -11.97, -10.06, -7.60, -2.78, -12.21, -11.55, -3.67, -10.63, +3.33, +5.15, -1.31, +5.83, 0.40, +5.98, -4.57, -15.24 ]
  q502 = [ +25.39, +24.12, +22.48, +10.48, +5.51, -1.65, +15.81, +21.77, +20.41, +6.50, +5.48, +6.57, -5.10, -6.46, -7.46, -18.54 ]
  q510 = [ -31.1, -13.4, +9.3, +11.6, -132.3, -158.7, -109.9, -76.0, -2.9, -9.10, -56.8, -39.2, -46.5, 0, 0, 0 ]
  q511 = [ +19.1, +23.7, +29.6, +34.8, -10.2, +13.2, +63.2, +43.2, +29.6, +12.2, -38.1, -29.1, -35.4, +5.5, +97.9, +128.2 ]
  q520 = [ -2529., -2529., -2529., -2529., -2529., -2529., -3625., -4353., -1675., -1341., -1705., -1284., -896., 0, 0, 0 ]
  q530 = [ 0, 0, 0, 0, 0, 0, 0, 0, 0, 0, 0, 0, 0, 0, 0, 0 ]
  q540 = [ -358.1, -358.1, -358.1, -78.6, +203.1, -155.3, -144.2, +23.6, +99.5, +129.3, +153.1, +218.0, +190.2, +276.6, 0, 0 ]
ENDIF ELSE BEGIN ; Lindegren
  gcut5 = [ 6.0, 10.8, 11.2, 11.8, 12.2, 12.9, 13.1, 15.9, 16.1, 17.5, 19.0, 20.0, 21.0 ]
  q500 = [ -26.98, -27.23, -30.33, -33.54, -13.65, -19.53, -37.99, -38.33, -31.05, -29.18, -18.40, -12.65, -18.22 ]
  q501 = [ -9.62, -3.07, -9.23, -10.08, -0.07, -1.64, +2.63, +5.61, +2.83, -0.09, +5.98, -4.57, -15.24 ]
  q502 = [ +27.40, +23.04, +9.08, +13.28, +9.35, +15.86, +16.14, +15.42, +8.59, +2.41, -6.46, -7.46, -18.54 ]
  q510 = [ -25.1, +35.3, -88.4, -126.7, -111.4, -66.8, -5.7, 0, 0, 0, 0, 0, 0 ]
  q511 = [ -0.0, +15.7, -11.8, +11.6, +40.6, +20.6, +14.0, +18.7, +15.5, +24.5, +5.5, +97.9, +128.2 ]
  q520 = [ -1257., -1257., -1257., -1257., -1257., -1257., -1189., -1404., -1165., 0, 0, 0, 0 ]
  q530 = [ 0, 0, 0, 0, 0, 0, 0, 0, 0, 0, 0, 0, 0 ]
  q540 = [ 0, 0, 0, 0, 0, 0, 0, 0, 0, 0, 0, 0, 0 ]
ENDIF ; Six-parameter solutions use Lindegren
  gcut6 = [ 6.0, 10.8, 11.2, 11.8, 12.2, 12.9, 13.1, 15.9, 16.1, 17.5, 19.0, 20.0, 21.0 ]
  q600 = [ -27.85, -28.91, -26.72, -29.04, -12.39, -18.99, -38.29, -36.83, -28.37, -24.68, -15.32, -13.73, -29.53 ]
  q601 = [ -7.78, -3.57, -8.74, -9.69, -2.16, -1.93, +2.59, +4.20, +1.99, -1.37, +4.01, -10.92, -20.34 ]
  q602 = [ +27.47, +22.92, +9.36, +13.63, +10.23, +15.90, +16.20, +15.76, +9.28, +3.52, -6.03, -8.30, -18.74 ]
  q610 = [ -32.1, +7.7, -30.3, -49.4, -92.6, -57.2, -10.5, +22.3, +50.4, +86.8, +29.2, -74.4, -39.5 ]
  q611 = [ +14.4, +12.6, +5.6, +36.3, +19.8, -8.0, +1.4, +11.1, +17.2, +19.8, +14.1, +196.4, +326.8 ]
  q612 = [ +9.5, +1.6, +17.2, +17.7, +27.6, +19.9, +0.4, +10.0, +13.7, +21.3, +0.4, -42.0, -262.3 ]
  q620 = [ -67., -572., -1104., -1129., -365., -554., -960., -1367., -1351., -1380., -563., +536., +1598. ]
  n = N_ELEMENTS(gmag)
  IF n NE N_ELEMENTS(nueff) OR n NE N_ELEMENTS(lat) OR n NE N_ELEMENTS(npar) THEN STOP, 'Incompatible data'
  c0 = 1.0 + FLTARR(n)
  c1 = -0.24*(nueff LE 1.24) + (nueff-1.48)*(nueff GT 1.24 AND nueff LE 1.72) + 0.24*(nueff GT 1.72)
  c2 = +0.24^3*(nueff LE 1.24) + (1.48-nueff)^3*(nueff GT 1.24 AND nueff LE 1.48)
  c3 = (nueff-1.24)*(nueff LE 1.24)
  c4 = (nueff-1.72)*(nueff GT 1.72)
  b0 = 1.0 + FLTARR(n)
  b1 = SIN(!DTOR*lat)
  b2 = SIN(!DTOR*lat)*SIN(!DTOR*lat) - 1./3
  gmagc = MIN(gcut5) > gmag < MAX(gcut5) ; Caps G between 6 and 21
  p = WHERE(VALID_NUM(gmagc) EQ 0, np)
  IF np NE 0 THEN gmagc[p] = 21.0 ; Stars with non-valid G are assumed to be faint
  qq500 = INTERPOL(q500, gcut5, gmagc)
  qq501 = INTERPOL(q501, gcut5, gmagc)
  qq502 = INTERPOL(q502, gcut5, gmagc)
  qq510 = INTERPOL(q510, gcut5, gmagc)
  qq511 = INTERPOL(q511, gcut5, gmagc)
  qq520 = INTERPOL(q520, gcut5, gmagc)
  qq530 = INTERPOL(q530, gcut5, gmagc)
  qq540 = INTERPOL(q540, gcut5, gmagc)
  qq600 = INTERPOL(q600, gcut6, gmagc)
  qq601 = INTERPOL(q601, gcut6, gmagc)
  qq602 = INTERPOL(q602, gcut6, gmagc)
  qq610 = INTERPOL(q610, gcut6, gmagc)
  qq611 = INTERPOL(q611, gcut6, gmagc)
  qq612 = INTERPOL(q612, gcut6, gmagc)
  qq620 = INTERPOL(q620, gcut6, gmagc)
  z5 = qq500*c0*b0 + qq501*c0*b1 + qq502*c0*b2 + qq510*c1*b0 + qq511*c1*b1 + qq520*c2*b0 + qq530*c3*b0 + qq540*c4*b0
  z6 = qq600*c0*b0 + qq601*c0*b1 + qq602*c0*b2 + qq610*c1*b0 + qq611*c1*b1 + qq612*c1*b2 + qq620*c2*b0
  out = z5*(npar EQ 5) + z6*(npar EQ 6) ; Returns zero for npar = 2 (or indeed any value other than 5 or 6)
  RETURN, out
END

```